ISSN 1753-3562

August 2017 Volume 58 Number 4

PHYSICS AND CHEMISTRY OF GLASSES

European Journal of Glass Science and Technology Part B

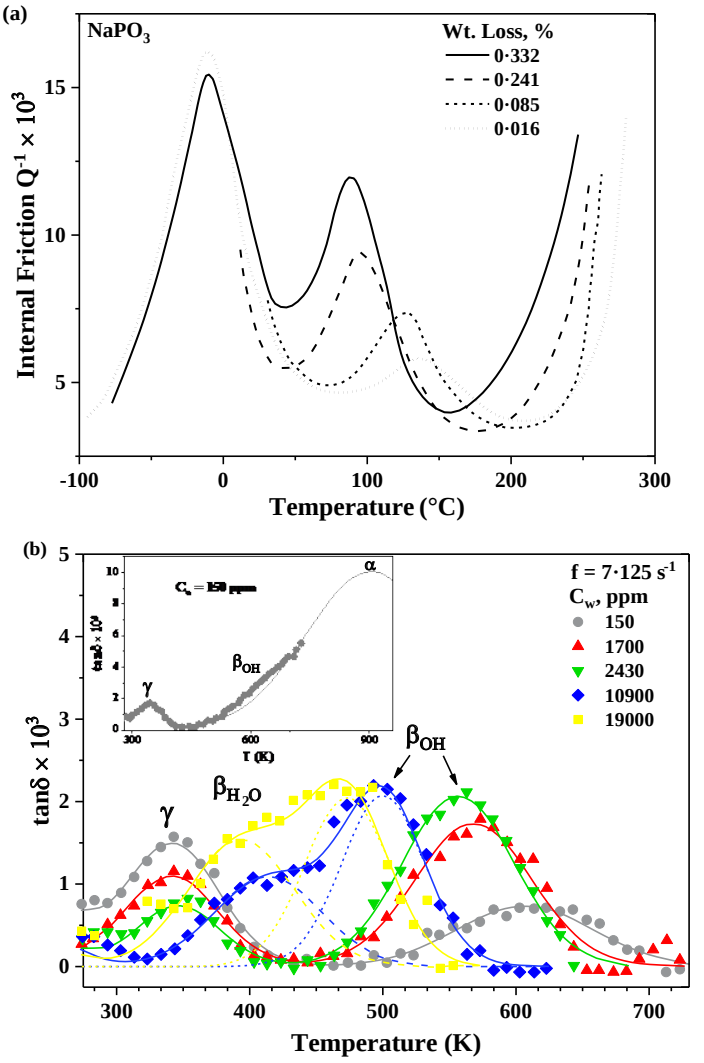

100 years of Society of Glass Technology journals

Volume 58 Number 4 **August 2017**

Physics and Chemistry of Glasses

European Journal of Glass Science and Technology B

CONTENTS

Cover: *(a) Internal friction loss peaks of sodium phosphate ($Na_2O–P_2O_5$) glass containing various amounts of water. The peak at ~100°C is due to water in glass. (b) Dynamic mechanical loss characteristics of soda–lime–silica glass with various water contents. There are loss peaks due to OH and H_2O in this glass. In both diagrams, the lowest temperature peaks are attributed to sodium motion in the glass. The role of water in surface stress relaxation of glass Minoru Tomozawa & Emily M. Aaldenberg, this issue, pages 156–164.*

The European Journal of Glass Science and Technology is a publishing partnership between the Deutsche Glastechnische Gesellschaft and the Society of Glass Technology. Manuscript submissions can be made through Editorial Manager, see the inside back cover for more details.

Society of Glass Technology
9 Churchill Way
Chapeltown
Sheffield S35 2 , UK
Tel +44(0)114 263 4455
Fax +44(0)8718754085
Email info@sgt.org
Web http://www.sgt.or

The Society of Glass Technology is a registered charity no. 237438.

Advertising
Requests for display rates, space orders or editorial can be obtained from the above address.

Physics and Chemistry of Glasses: European Journal of Glass Science and Technology, Part B
ISSN 1753-3562 (Print)
ISSN 1750-6689 (Online)

The journal is published six times a year at the beginning of alternate months from February.

Electronic journals: peer reviewed papers can be viewed by subscribers through Ingenta Select
http://www.ingentaconnect.co

Claims for free replacement of missing journals will not be considered unless they are received within six months of the publication date.

Influence of phase separation on structure–property relationships in the $(GeSe_2–3As_2Se_3)_{1–x}PbSe_x$ glass system

Anupama Yadav,[*1] *Myungkoo Kang,*[1] *Charmayne Smith,*[1] *Jason Lonergan,*[1] *Andrew Buff,*[1] *Laura Sisken,*[1] *Karima Chamma,*[1] *Cesar Blanco,*[1] *Joe Caraccio,*[1] *Theresa Mayer,*[2] *Clara Rivero-Baleine*[3] *& Kathleen Richardson*[*1]

[1] *College of Optics and Photonics, CREOL, University of Central Florida, Orlando, FL 32816, USA*
[2] *Virginia Polytechnic Institute and State University, Blacksburg, VA 24061, USA*
[3] *Lockheed Martin Corporation, Orlando, FL 32819, USA*

The physical properties of chalcogenide glasses in the $(GeSe_2–3As_2Se_3)_{1–x}PbSe_x$ [GAP-Se] series (x=0–55 mol%) have been measured as a function of PbSe content and glass morphology. Measurements of density, microhardness, thermal properties (glass transition, stability and conductivity) and IR transmission spectra have been correlated with Pb content illustrating the impact of liquid–liquid phase separation (LLPS) on properties within this multicomponent chalcogenide glass system. The role of Pb as both a modifier and network participant is proposed as a structural interpretation of property variation across the series. Density, microhardness and thermal conductivity showed an increase with PbSe content whereas glass transition temperature (T_g) exhibits a minimum near the center of the immiscibility zone correlated to a decrease in glass stability when a Pb-rich matrix is present. The structural origin of the change in the properties is confirmed using Raman spectroscopy and transmission electron microscopy (TEM) which illustrate the different morphology of phase separation present and how it impacts property evolution.

1. Introduction

Chalcogenide glasses (ChGs) have drawn great interest for their unique optical properties but are often limited by their weak thermal and mechanical properties.[1–3] With unique properties not exhibited by homogeneous glasses or mono- or polycrystalline ceramics, glass-ceramics (GCs) are often the preferred choice of materials in many technical, optical, medical, electrical and architectural fields.[4–8] Additional uses of GCs include unique materials for coatings and laser applications.[9,10] The attributes of glass-ceramic materials are defined by the microstructure and composition of the crystalline phase and the (parent) glassy matrix phase developed during the manufacturing process. The ability to control the properties of both phases depends on the initial glass composition and by the heat treatment protocol used to convert glass to a glass-ceramic. Numerous references describe how this has been employed in commercial applications. [11–15]

Phase separation effects are of general interest in glass science, as it can give rise to pronounced changes in physical, thermal and optical properties of network glasses which may be useful or detrimental.[16,17] Detailed characteristics of phase separated glasses depend strongly on the nature and volume fraction of the phases developed. Most commercial glass-ceramic systems utilize homogeneous phase separation, as nucleation sites, to ensure heterogeneous nucleation to produce a rapidly nucleating glass ceramic via a reduced activation energy for crystallization. Recent efforts to deliberately define 'phase separable', multicomponent glass compositions which serve as a process route to making fully crystallized transparent ceramics, have shown promise with an ability to control crystal size and other attributes important for their use in optical applications (i.e. rare earth solubility, scatter),[18] or for engineering the linear and nonlinear optical properties of optical components.[19] Related efforts examining infrared (IR) glass-ceramics have been reported which may or may not (deliberately) exploit phase separation as a stepping stone to controlled crystallization.[13,14,20]

Oxide and non-oxide glasses possess compositions known to exhibit phase separation, though literature on specific aspects in non-oxide systems (such as phase diagrams and immiscibility boundaries) is limited with a few noteworthy exceptions.[21] As discussed below, such glass compositions possess large, positive enthalpies of mixing in the liquid state resulting in instability that can vary with composition. This results in the bulk liquid's separation into two different amorphous phases upon quenching from the melt (typically well above T_c, the consolute

* Corresponding authors. Email kcr@creol.ucf.edu, yadav.anupama@knights.ucf.edu
Original version presented as an Invited Paper at the Turner Legacy Symposium within the programme of the Society of Glass Technology Centenary Conference and 13th Symposium of the European Society of Glass Science and Technology, Sheffield, UK, 4–8 September 2016.
DOI: 10.13036/17533562.58.4.115

or critical temperature) to room temperature. This 'de-mixing' can be stable, unstable or metastable, depending on where the immiscibility dome resides in composition/temperature space, with respect to the melt's liquidus temperature, T_L.[22] As recently summarized for a variety of compositions and applications in an excellent review,[23] phase separation models are varied and largely have been used to explain mechanistic processes (diffusion-based, classical nucleation and growth, and more recently, those based on structural considerations)[24] and will be only briefly discussed here.

There are two generally accepted mechanisms for the phase separation in glasses: nucleation-growth and spinodal decomposition.[25] Both are derived from thermodynamic instabilities created by free energy differences during mixing when the temperature-dependent entropy is not large enough to offset a positive enthalpy of mixing, ΔH_m. This results in a deviation from complete miscibility (a minimum in ΔG_m) and the resulting de-mixing or immiscibility presents itself. The extent of immiscibility is temperature dependent and there is usually a critical temperature (T_c), at the top of the immiscibility 'dome' depicted (where known on phase diagrams) below which de-mixing occurs. The glass microstructure or morphology developed from each mechanism will be quite different, thus impacting physical properties, differently. For purposes of this study, we will refer to systems of liquid–liquid phase separation (LLPS) as having varied *morphology*, i.e. when there are multiple amorphous phases present, unless there is evidence of crystallization (where we will refer to the material as having a variation in *microstructure* consisting of amorphous and crystalline phases).

The nucleation-growth mechanism typically results in a glass morphology consisting of isolated spheres of one equilibrium composition randomly dispersed as 'droplets' through a matrix of another equilibrium composition. Phase separation by a nucleation and growth mechanism is expected to proceed when a system leaves the thermodynamically *stable* condition and enters the metastable region of the phase diagram, between the binodal and spinodal curve. For spinodal decomposition, a very fast transition is required to move the system from the stable region to the unstable spinodal phase region, through the metastable nucleation region of the phase diagram. Spinodal decomposition (typically) results in a three-dimensionally interconnected morphology consisting of two immiscible phases.

Recently, the phenomenon of creating amorphous–amorphous phase separated chalcogenide glasses has generated considerable attention, in efforts to create infrared transparent glass-ceramics.[13,14,26] While reports of the liquid–liquid phase separation (LLPS) in chalcogenide glasses exist,[16,27–29] composition-dependent data and specific thermodynamic and kinetic conditions/phase diagrams associated with such occurrences is limited. Depending on the glass composition, droplet-matrix type or interconnected spinodal morphology has been reported within the immiscibility dome in chalcogenide systems.[30,31]

Previous studies of glasses exhibiting phase separation and that are then used as glass-ceramics have shown that by incorporating PbS, PbSe, or CdSe, crystallization behaviour can be affected through "self-nucleation".[31–35] It is well known that chalcogenide glass-ceramics containing microcrystals can have a low coefficient of thermal expansion and improved thermal and mechanical properties. Here, the droplets formed can serve as an isolated composition wherein crystallization can occur in a spatially defined manner. Such crystallization leads to modification of resulting physical properties in the glass-ceramics. As seen in the $GeSe_2$–As_2Se_3–CdSe system, the introduction of CdSe leads to an increase in the density, glass transition temperature and microhardness of the glasses, at the expense of a decrease in thermal stability of the glass with CdSe content. The generation of a secondary crystalline phase has also been demonstrated in alkali or metal halides systems such as in $GeTe_4$–$AsTe_3$–AgI glasses.[36] Here, AgI addition was shown to increase the glass forming ability and thermal stability of the glass matrix. The resulting microcrystallized glasses exhibited improved mechanical properties while maintaining the transmission domain of 2 to 25 μm. Efforts in the ternary Ge–Ga–S system suggests that phase separation may play a role crystallite growth process employed in the resulting transparent glass-ceramic as evident in papers by Lin *et al*, where the secondary crystalline phase ($GeSe_2$) was believed to have initiated within droplets.[37,38]

Infrared glass-ceramics for low loss optical applications require small and finely dispersed crystalline phase, preferably with low absorption loss and refractive index to avoid light scattering. This can be achieved by selecting a glass that precipitates a single (or few) crystalline phase(s) of similar index upon devitrification, that is cubic and exhibits a narrow crystallite size distribution. Early studies in the $GeSe_2$–As_2Se_3–PbSe composition space have shown that addition of PbSe in the glass network can produce small, interconnected spinodal morphology.[32,33] In these systems high $GeSe_2$ glasses usually have better rigidity and chemical durability and in particular, longer IR cut-off wavelength, whereas high As_2Se_3 glasses are good glass formers and possess high thermal stability and a near-zero thermo-optic coefficient. While both $GeSe_2$ and As_2Se_3 glasses have been studied extensively for many optical applications, very few works have focused on the properties of these glasses containing PbSe, across a broad region of morphology variation. In this study, physical, thermal, and optical properties

of the $(GeSe_2–3As_2Se_3)_{1-x}PbSe_x$ glass system is studied. These glasses have been examined in our group for use in IR transparent nanocrystalline glass-ceramics. As will be presented, some compositions within the x=0–55 mol% PbSe series exhibit LLPS prior to the heat treatment schedule required to convert them to glass-ceramics. This impacts not only their transparency but also their other physical properties. We review the role of Pb in this Ge–As–Pb–Se glass network and correlate that role to the observed material morphology and resulting physical properties.

2. Experimental

Bulk chalcogenide glasses (compositions listed in Table 1) of $(GeSe_2–3As_2Se_3)_{1-x}PbSe_x$ [GAP-Se] with varying PbSe concentrations (0 to 55 mol%) were prepared by conventional melt-quenching technique. All glasses were prepared using high purity raw materials (metals basis) from Alfa-Aesar: selenium (99·999%), germanium (99·999%), antimony (99·999%), and lead (99·999%). These elements were carefully weighed and batched in a nitrogen purged MBraun Labmaster 130 glove box. The weighed batches (40 g) were loaded into cleaned fused quartz tubes and sealed under vacuum using a methane–oxygen torch to form sealed ampoules. The batches were melted in a rocking furnace overnight at a melting temperature, T_m=850°C. After overnight rocking at elevated temperature, the furnace was then cooled to the quench temperature, T_Q=650°C, prior to removal from the furnace for quenching using compressed air flowing over the ampoule. The quench rate for this method is estimated to be ~120°C/min. To minimize the quench-related stress, glasses were annealed at 177°C for 2 h and cooled to room temperature. The prepared glass rods were removed from the ampoules and cut into slices of thickness ~2 mm using a slow speed saw. Grinding was done with silicon carbide grinding paper with fine grit sizes. For optical characterization, slices were subsequently polished on both sides using a polishing pad with 0·05 μm Al_2O_3 slurry.

To determine the morphology and chemical composition of the glasses, transmission electron microscopy (TEM) cross-sectional specimens were prepared by focused ion beam-assisted milling followed by lift-out processing in a FEI Helios Nanolab 660 focused ion beam. The specimens were mounted on Cu grids and ion polished to ~50 nm thickness for electron transparency. TEM imaging and selected area electron diffraction (SAED) measurements of the cross-sectional specimens were carried out using a Talos F200X at 200 kV. X-ray energy dispersive spectroscopy (XEDS) data were collected using scanning transmission electron microscopy (STEM) in the Talos F200X at 80 kV to assess any chemical segregation within the glass matrices.

Table 1. Batch Compositions of GAP-Se samples under study

Sample	*Mole % (as batched)*			*Atomic % (as batched)*			
	$GeSe_2$	*As_2Se_3*	*PbSe*	*Ge*	*As*	*Pb*	*Se*
0	25·0%	75·0%	0%	5·6%	33·3%	0·0%	61·1%
5	23·8%	71·3%	5%	5·4%	32·6%	1·1%	60·9%
10	22·5%	67·5%	10%	5·3%	31·8%	2·4%	60·6%
15	21·3%	63·8%	15%	5·2%	30·9%	3·6%	60·3%
20	20·0%	60·0%	20%	5·0%	30·0%	5·0%	60·0%
25	18·8%	56·3%	25%	4·8%	29·0%	6·5%	59·7%
30	17·5%	52·5%	30%	4·7%	28·0%	8·0%	59·3%
35	16·3%	48·8%	35%	4·5%	26·9%	9·7%	59·0%
40	15·0%	45·0%	40%	4·3%	25·7%	11·4%	58·6%
45	13·8%	41·3%	45%	4·1%	24·4%	13·3%	58·1%
50	12·5%	37·5%	50%	3·8%	23·1%	15·4%	57·7%
55	11·3%	33·8%	55%	3·6%	21·6%	17·6%	57·2%

The amorphous nature of all samples was confirmed by powder x-ray diffraction (XRD) as recorded by a PANalytical Empyrean XRD unit. X-ray diffraction was performed at room temperature in a continuous scan mode, operated at 40 kV and 40 mA, with a range of 2θ between 10° and 70°.

The structural properties of the glasses were investigated using a Bruker Senterra micro-Raman spectrometer. Raman scattering measurements were performed with an excitation laser wavelength of 785 nm with 1 mW power. Data were collected using a 30 s exposure and was accumulated over five scans. Raman spectra in the range of 100 to 900 cm^{-1} were recorded. Measurements were repeated at different points on each glass sample to ensure that the Raman spectra measured were representative of the whole glass and that no photo-structural modification was induced in the material, during measurement.

The glass' physical properties including density and Vickers microhardness, were measured to evaluate how the bulk glass properties changed as a result of PbSe content and any observed morphological effects (LLPS). Density was measured using the Archimedes principle with distilled water as immersion fluid at room temperature. Vickers microhardness, V_H, measurements were performed on a Shimadzu DUH-211S Hardness Tester. Indentations were created on polished sample surfaces using a 100 mN load with a hold time of 10 s using a diamond indenter. The hardness tester was calibrated using a Ni metal calibration standard provided by Shimadzu. Sources of error can occur during this measurement if the sample does not have perfectly parallel surfaces (i.e. wedge) or if there is extensive pre-existing surface damage (cracks or scratches). The applied load was chosen to be below the point where indentations created cracks emanating from the corners of the indent.

Thermal analysis of each glass was carried out using a Netzsch DSC 204 F1 Phoenix differential scanning calorimeter (DSC). Small powder samples of ~15–20 mg were loaded into sealed aluminium pans. The samples were heated at a rate of 10°C/min from 25°C to 350°C. The glass transition temperature (T_g) was recorded as the point of inflection of the DSC

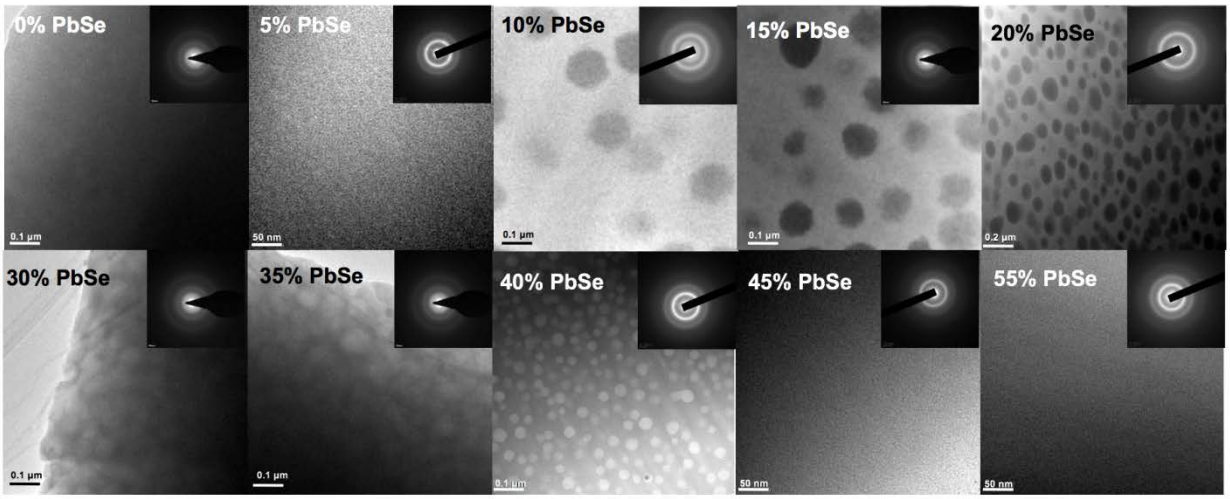

Figure 1. TEM images of selected glasses from the $(GeSe_2–3As_2Se_3)_{1-x}PbSe_x$ [GAP-Se] series with x=0, 5, 10, 15, 20, 30, 35, 40, 45 and 55 mol% PbSe concentration

curves of the low temperature endothermic feature. The temperature interval ΔT between the glass transition temperature (T_g) and the onset crystallization temperature (T_x) is considered as an indicator of glass stability where $\Delta T=T_x-T_g$. Glass stability was quantified based on each sample's ΔT as a function of composition.

Thermal conductivity was measured on bulk samples using the transient plane source (TPS) method (ThermTest, TPS 3500, Fredericton Canada).[39] The TPS method has been shown to be a precise and convenient method for measuring the thermal transport properties of bulk chalcogenide glasses.[40,41] This method utilizes a planar sensor in the form of a double spiral of electrically conducting nickel (Ni) metal sandwiched between two samples of the glass under study, where each sample is polished to a thickness of ~2·0 mm. During the measurement, a constant current passes through the conducting sensor which increases the temperature of the sensor. The heat generated dissipates into the samples located on both sides of the sensor, at a rate that depends on the thermal transport properties of the material.

Transmission spectra were recorded on samples using a Perkin Elmer Frontier (visible-NIR) and a Perkin Elmer Frontier Optica (NIR-LWIR) Fourier transform infrared (FTIR) spectrometer. Measurements were averaged over 21 scans in the spectral range of 0·6 to 22 μm with resolution of 8 cm^{-1} at room temperature. During measurements, samples were mounted on a sample holder with a 3 mm aperture.

Further optical properties of these glasses including refractive index, dispersion, scattering and thermo-optic properties, have been evaluated in a separate article that tracks the base glass attributes and the impact of LLPS on key optical properties both prior to and following thermal treatment to realize infrared glass ceramics.[42] Additionally, the impact of how phase separation in GAP-Se scales with melt volume and varying thermal history for selected GAP-Se compositions, is also discussed separately.[43]

3. Results and discussion

3.1 Morphological variation with PbSe content: evidence of liquid–liquid phase separation (LLPS)

As discussed previously, chalcogenide glasses in the Ge–As–Pb–Se glass forming region (molar ratio of constituents Ge:As:Pb:Se=1·05:0·35:0·3:2·4) investigated by Mecholsky and co-workers in the early 1970s showed evidence of the presence of metastable phase separation characterized by large droplet-matrix morphology with other regions of spinodal decomposition.[27–29] The size scale of these inhomogeneities and the refractive index differences associated with their compositional variation gave rise to optical scattering which limited the optical transmission through the part. While well away from the Ge:As:Pb:Se ratio of these glasses, compositions in our study (network former molar ratios of Ge:As=1:6) showed regions of compositional homogeneity (no phase separation) at PbSe levels between 0–10 mol% and ~45–55 mol%. At intermediate levels (10<PbSe<40 mol%) glasses exhibited evidence of LLPS as characterized by a distinct droplet-matrix morphology and possibly, spinodal decomposition (25<x<~35 mol%). Figure 1 shows nanoscale images (bars=50, 100, or 200 nm) of the selected base glasses with varying PbSe concentration of 0, 5, 10, 15, 20, 30, 35, 40, 45 and 55 mol%, including bright field (BF) TEM images and SAED patterns. As can be seen, the Pb-free glass is homogeneous. For the low PbSe concentration of 5 mol%, the featureless TEM image and the corresponding diffuse SAED pattern indicate that the composition remains completely homogeneous and amorphous. For higher concentrations between 10–40 mol%, the TEM images

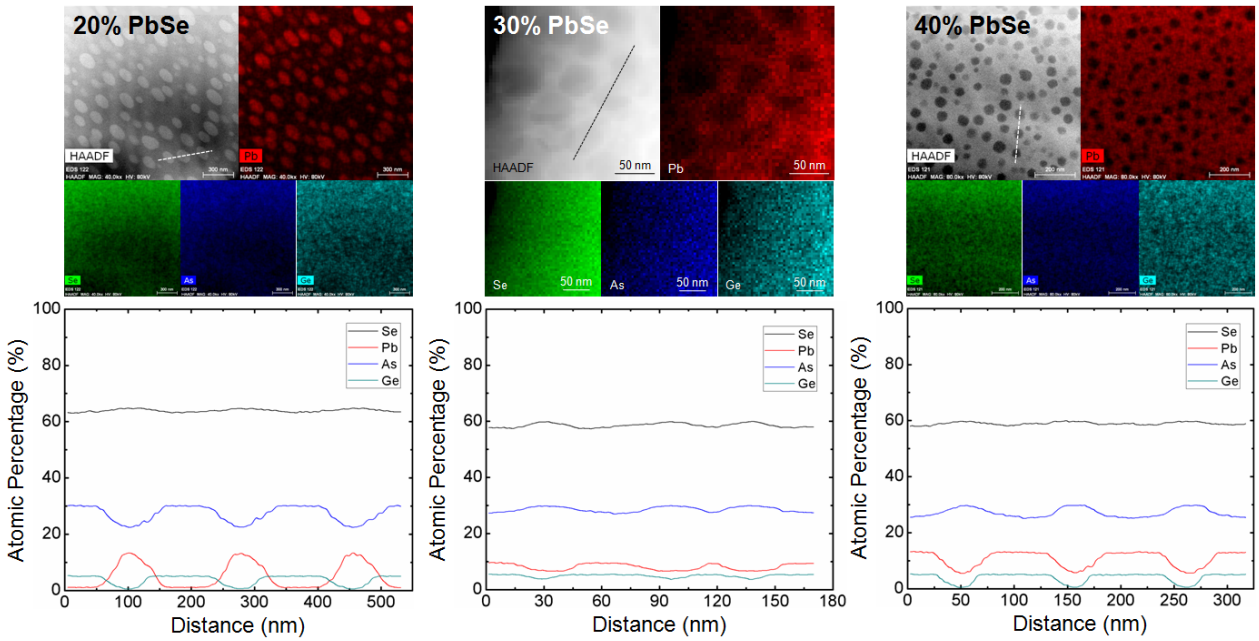

Figure 2. (top) DF STEM images, corresponding XEDS maps, and (bottom) linear composition profiles of three representative compositions with 20, 30 and 40 mol% of PbSe

show two distinct phases with a clear droplet-matrix morphology, and the corresponding SAED patterns confirm LLPS with both phases amorphous. The droplets have uniform, spherical shape and their sizes range from ~50 to ~130 nm. The contrasts between the droplet and the matrix regions in the BF TEM images are due to atomic mass variations. For example, as can be seen in the 20 and 40 mol% PbSe images, the 20% glass exhibits Pb-rich (heavier) droplets uniformly dispersed in a lighter (Pb-deficient) matrix. The converse is the case with 40 mol% PbSe. One can observe that the 20% composition exhibits spherical as well as non-spherical (elliptical) shaped droplets, indicative of a gradual shift towards a transition to spinodal. The irregular shaped bright regions in the 30 and 35% exhibit less compositional contrast and are likely with the region of spinodal decomposition. By 40 mol%, the droplet-matrix morphology has returned, with now Pb-deficient spherical drops clearly visible. For the highest PbSe samples (x=45, 50 and 55 mol%) the compositions were found to be homogeneous and amorphous with no evidence of immiscibility. Glasses above 55% PbSe in the series, crystallized upon quenching. No segregation or evidence of metallic lead was observed in any of the bulk glass samples.

Figure 2 shows dark field (DF) STEM images, corresponding XEDS maps, and linear composition profiles of representative compositions with 20, 30 and 40 mol% of PbSe. These three glasses in the series are believed to span the transition region from metastable to unstable to metastable phase separation. A clear transition in the chemical compositions of droplets, matrix and interconnected secondary phase can be seen in Figure 2. For these compositions, the distributions of Pb in the XEDS maps clearly match with those of the bright phase in the DF STEM images, suggesting that Pb atoms are segregated into the droplets (or the matrix) for the composition with 20 (40) mol% of PbSe, whereas in the 30% composition, the two phases are close in composition, as evident in the line-scan data. These results are very consistent with the atomic mass-induced contrasts observed in the BF TEM images. To quantify the atomic percentages of the four constituent elements in the amorphous glass matrices, linear composition profiles were extracted by making line scans across several droplet-matrix regions. The compositions for each region, compared to that of the batched composition are listed in Table 2. For the composition with 20 mol% of PbSe, the droplets and the matrix have average Pb atomic percentages of ~12·3 and ~1·7%, respectively, while those values are ~6·5 and ~ 9·5% for 30 mol% PbSe and ~13 and 7·3% for the droplet and matrix compositions within the 40 mol% of PbSe. As can be seen by the long line-scans that traverse multiple droplets, the droplet size is quite uniform and the within droplet-within matrix Ge:As:Pb:Se

Table 2. Atomic composition of 20, 30 and 40 mol% PbSe GAP-Se glasses

Composition		*Element* *Se*	*Pb*	*As*	*Ge*
20 mol%	Batch	60·0%	5·0%	30·0%	5·0%
	Secondary phase	64·3%	12·3%	22·1%	1·3%
	Matrix	62·8%	1·7%	29·8%	5·7%
30 mol%	Batch	59·3%	8·0%	28·0%	4·7%
	Secondary phase	59·9%	6·5%	29·8%	3·8%
	Matrix	57·7%	9·5%	27·3%	5·5%
40 mol%	Batch	58·6%	11·4%	25·7%	4·3%
	Secondary phase	57·9%	7·3%	31·3%	3·5%
	Matrix	60·2%	13·0%	23·9%	4·9%

ratios, are quite uniform. No evidence of secondary de-mixing (within the matrix phases of each) are evident based on comparison of the other Ge, As and Se XEDS maps. The droplet chemistry does however clearly show indications of deficiency in the network formers Ge and As (in the 20% sample) as compared to Ge and Pb deficiencies and As excess, in droplets within the 40% sample. These chemistry variations give insight into the likely crystallization products that might form in the droplets (20%) and matrix (40%), respectively, due to the reduced stability ($\Delta T=T_x-T_g$) of these respective Pb-enriched phases.

These microscopic observations suggest that the LLPS observed in this composition series exists over the composition range examined (10–40%). We arrive at this conclusion based on the following observations. Firstly, we observed the de-mixing to be stable up to very high temperatures, where rapid quenching protocols on varying melt sizes (ranging from small (25 g) to large (400 g)) all exhibited droplet-matrix morphology (with varying droplet sizes but similar compositions). In searching for the critical temperature (T_c) above which we might expect to see a homogeneous melt that gives rise to a homogeneous glass, none was observed up to melt temperatures of 950°C. Glasses removed from the furnace at these high melting temperatures were boiling and extensive vapour filled the tube. Thus, no higher temperatures were employed. To compare morphology and properties directly, all glasses prepared for evaluation were of constant melt volume and saw the same melt/quench thermal history. Secondly, both droplet matrix and spinodal morphologies can be seen in the TEM data shown. Unstable or metastable LLPS is observed in the central region of the immiscibility dome where we believe spinodal morphology is present. This was observed directly via TEM in the 30 and 35 mol% glass as the droplet phase in these glasses is less distinct in shape, looking more coarse and irregular. This is consistent with an interconnected dual phase morphology with a subtle but measurable composition variation as shown in Figure 2 and quantified in Table 2. As shown in the compositional line scan obtained with XEDS across the bright and dark features of the dual amorphous phases (line scans across the two phases shown in the central panel of Figure 2), the sharp droplet/matrix contrast in phase composition is not observed suggesting that the 30 mol% composition is clearly near composition regime where the cross-over from Pb-deficient to Pb-rich matrices, occurs. This compositional transition region can be seen in the line scan for the 30% glass as indicated by the slowly varying chemistry change and in the bright/dark image contrast (indicative of a less sharp boundary between phases). This plateau is distinctly different from the sharp droplet/matrix compositional heterogeneity of the 20 and 40% glasses, quantitatively shown in the secondary and

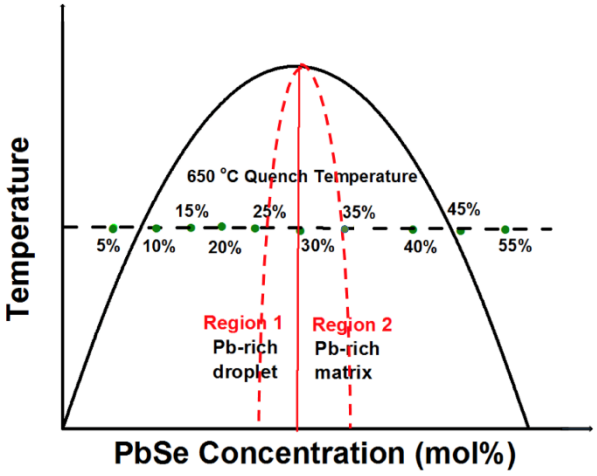

Figure 3. Schematic diagram for the proposed immiscibility dome in the $(GeSe_2–3As_2Se_3)_{1-x}PbSe_x$ [GAP-Se] glass system. Diagram shows the different compositions examined and their position within the various regions of the phase diagram, as well as the approximate point of transition to spinodal decomposition (within the red dashed lines) from the adjacent droplet-matrix morphology. While no temperature scale values are known, phases were shown to exist up to quench temperatures of 950°C [Colour available online]

matrix compositional summaries in Table 2 for the two phases of the 30% glass, is observed as well in some of the physical property trends discussed below where the usual dominant matrix phase morphology, is not distinctly present.

Based upon the observed morphological transitions and the chemical compositions of the droplet and matrix phases shown in Figures 1 and 2, the occurrence of phase separation is estimated to be confined within a region of ~10 and ~40 mol% of PbSe, as illustrated in the schematic diagram of our proposed immiscibility dome (Figure 3) where the green spots correspond to the compositions in Figure 1. The dashed red (centre) region of the schematic illustrates the boundaries where the transition from droplet-matrix morphology changes to spinodal, and then back to droplet/matrix at higher PbSe content. The impact of this morphology variation plays heavily on the resulting structural and physical property variations observed as discussed in subsequent sections.

Figure 4 shows FTIR spectra of selected samples measured at room temperature in the spectral range from 0·6 to 22 μm. Homogeneous glasses (0 and 50 mol%) exhibit the expected decrease in transmission based on increased refractive index (and hence, Fresnel loss) associated with the addition of a highly polarizing Pb atom. Additionally, the progress of decrease in internal transmittance with PbSe content also highlights this increase in refractive index, as well as evidence of oxide impurity imparted into the glass with Pb addition. This absorption, shown as a

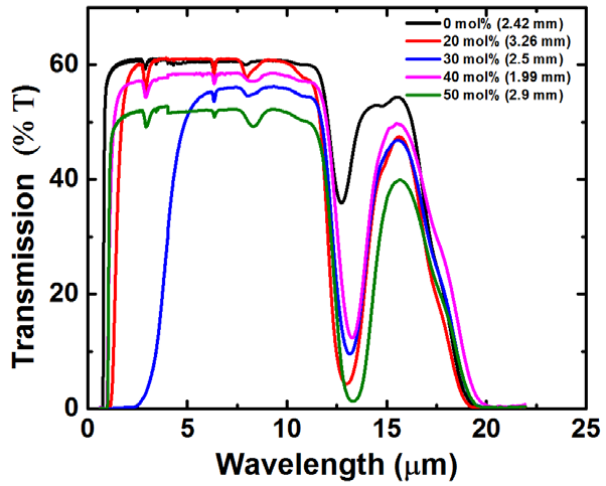

Figure 4. IR-transmission spectra of the selected glasses (0, 20, 30, 40 and 50 mol% PbSe (thickness of the sample)) exhibiting signatures consistent with the composition and morphological variation. Spectra are not corrected for Fresnel loss

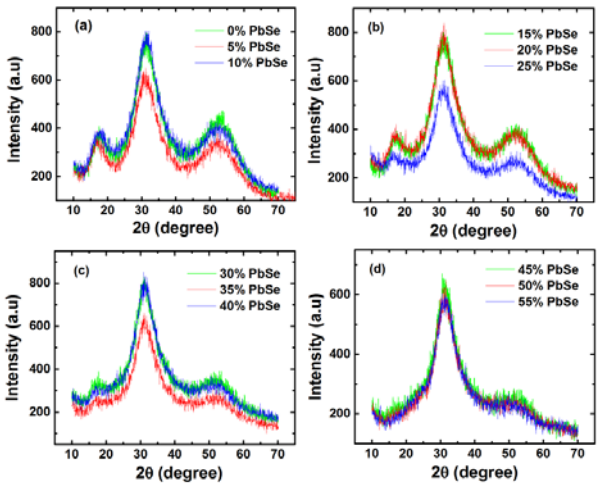

Figure 5. XRD patterns of as-quenched glasses within the $(GeSe_2–3As_2Se_3)_{1-x}PbSe_x$ [GAP-Se] series with x=0 to 55 mol% PbSe

deep decrease in transmission in the ~12 μm region, increases monotonically with Pb content and is likely attributed to the elemental Pb starting material quality. Intermediate Pb-containing glasses show transmission dominated by their respective matrix phase: in glasses <30 mol% PbSe, this is a Pb-deficient phase which exhibits higher transmission as Pb is concentrated in the small droplets (typically <100 nm in size) and in a Pb-rich matrix for glasses with 35 mol% PbSe or greater. Glass compositions in these two regions adjacent to the centre of the immiscibility dome show the most phase separation as characterized by their BF contrast, deviation from batched composition and large droplet size. For the 30 mol% PbSe composition situated near to the believed transition boundary where a higher contrast droplet-matrix morphology transitions to a more spinodal-like morphology, the Pb is more integrated in both phases. This results in a lower transmittance for the 30 mol% PbSe glass, which also shows a distinct red-shift is observed for the short-wavelength edge of the transmission spectra. While the compositional variation between the two amorphous phases is smaller than in the droplet-matrix compositions (as indicated by the centre panel in Figure 2), the interface area of the three dimensionally interconnected phases may likely be larger, giving rise to high scattering. The clear blue-shift seen in the 40 mol% glass is additional evidence that this glass (30 mol%) resides within the spinodal region where as validated by the TEM and XEDS data in Table 2. As the 30% glass' composition does not contain droplets and the two phases are very similar in composition with the Pb more evenly dispersed throughout the glass as compared to the adjacent droplet-matrix (20 and 40%) containing glasses, it is believe that the shift in the short wavelength edge of the glasses is largely dominated by scattering effects from the larger fraction of interfaces between the inter-twined phases of differing refractive indices.[42] FTIR short wavelength edge shift measurements combined with the compositional data from XEDS provides a sensitive method for detecting the extent of the liquid–liquid phase separation.

3.2 Compositional dependence of PbSe on glass network

Figure 5 shows the XRD patterns of all glass samples. The measured XRD patterns confirm the x-ray amorphous nature of all the glasses from 0 to 55 mol% of PbSe concentration with no evidence of crystallization. These data infer that above ~30 mol% PbSe, there exist two primary glass-forming matrix units that dominate the glass' network. As we believe this to be the onset region of a Pb-rich matrix with small (lower volume fraction) Pb-deficient droplets, it is consistent that the patterns possess two distinct 2θ features with similar shapes, across this composition space. Conversely, below this level, $GeSe_2$ and As_2Se_3 dominate the glass network (with again, a small volume fraction of a Pb-rich droplet phase) possibly contributing to the more detailed (three primary amorphous humps) XRD patterns.

To further evaluate the impact of the LLPS morphology on the glass network's structure, micro-Raman analysis was carried out. Figure 6 shows the measured room temperature Raman spectra for various compositions. For convenience of comparison, the entire frequency range of Raman spectra from 100 to 900 cm^{-1} is divided into two regions with individual figures. Note that while the wavenumber scale is consistent across all vertical figures, the Y-axis of intensity is not. The spectra of all the compositions for the frequency range between 100 and 400 cm^{-1} is shown in Figures 6(a1, b1, c1 and d1); whereas data

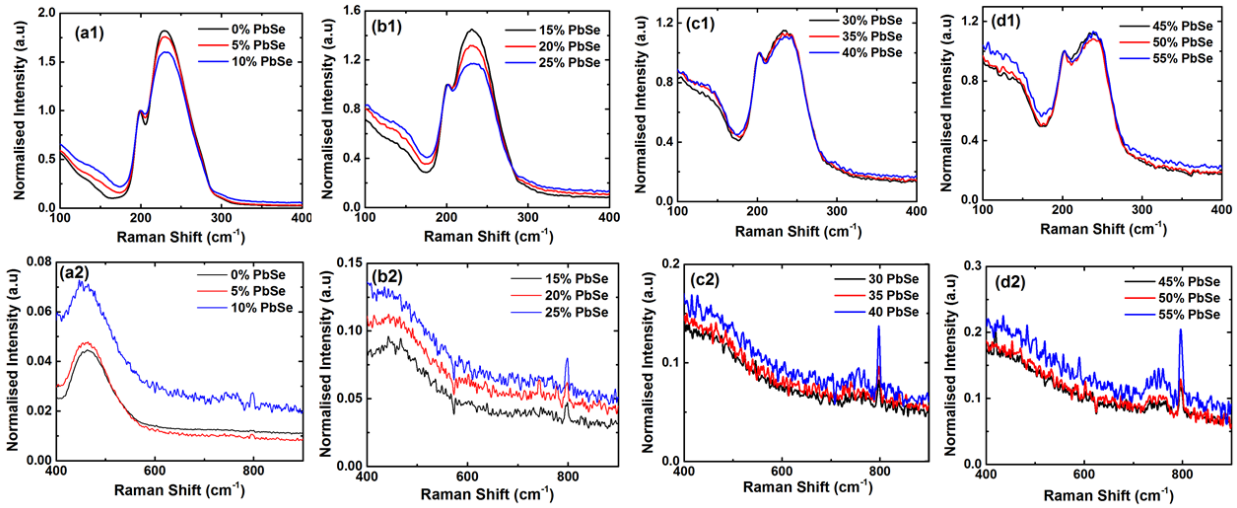

Figure 6. Raman Spectra of $(GeSe_2–3As_2Se_3)_{1-x}PbSe_x$ [GAP-Se] glasses with varying concentration of PbSe

for the range between 400 and 900 cm^{-1} is given in Figures 6(a2, b2, c2 and d2). To examine the evolution of various bands with PbSe concentration, the entire Raman spectra from 100 to 900 cm^{-1} has been normalized to the band at 200 cm^{-1}.

We attribute the bands within these spectra to the dominant glass network bands associated with each composition. $GeSe_2$ has the structural unit of $A'B_4$ tetrahedron with four-fold coordinated Ge at the centre. The tetrahedron is interconnected by the two-fold coordinated Se atom. Similarly, for As_2Se_3 the structural unit is AB_3 pyramid with three-fold coordinated As atom at the apex. The pyramids are interconnected by the two-fold coordinated Se atom. The low frequency vibration mode of the Ge–Se bonds in $GeSe_4$ corner sharing tetrahedral attributes to the peak located at 200 cm^{-1}.[44,45] The nearby peak at 230 cm^{-1} is typical of the vibrational frequency of the $AsSe_{3/2}$ pyramidal structural units.[46,47] Comparison of Raman spectra for compositions within the PbSe series, clearly shows that structural changes occur in the glass due to incorporation of PbSe. Introduction of PbSe into network induces three major changes in the Raman Spectra, which can be seen in Figure 6 and are more distinctly in Figure 7 which tracks the primary peaks in the spectra. What can be observed as a function of PbSe content is firstly, the appearance of a peak at 800 cm^{-1}, second is the decrease in the peak intensity of 230 cm^{-1} and third is the rise in the peak intensity of 800 cm^{-1}.

While the PbSe is not Raman active, its formal association with other network species (Ge–As–Se) gives rise to a signature. The high frequency peak that appeared at about 800 cm^{-1} is in accordance with the polar theory reported for PbSe, which possibly corresponds to the ground state energy of the PbSe polaron.[48–50] This peak is not seen for 0 mol% PbSe.

It can readily be seen from the Raman spectra of the PbSe-free $GeSe_2–3As_2Se_3$ (0 mol% PbSe) glass and the PbSe substituted system that the intensity of the peak at 230 cm^{-1} decreases successively with the increasing PbSe concentration and remains constant

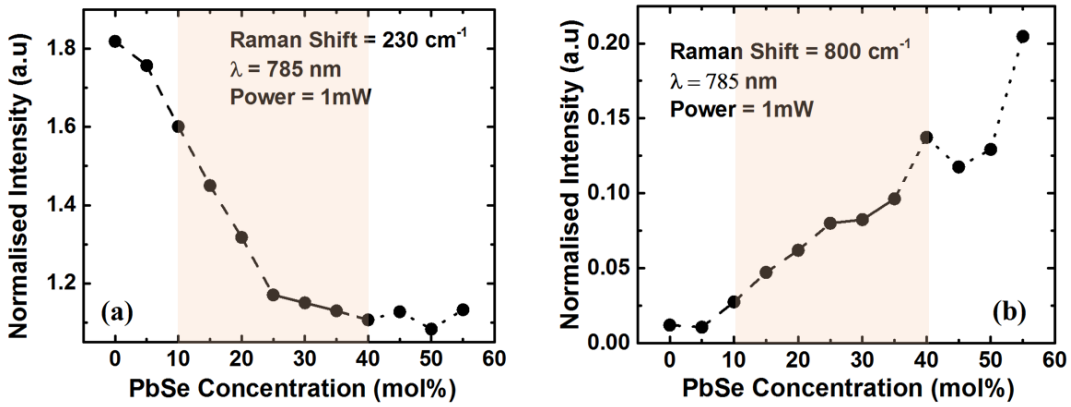

Figure 7. (a) Decrease in the Raman Intensity of 230 cm^{-1} peak as function of PbSe concentration. (b) and (c) shows the rise in the peak of 800 cm^{-1} and 1250 cm^{-1} with increase in PbSe concentration. The shaded area ($10 \leq x \leq 40$ mol% PbSe) indicates the composition where phase separation was observed by TEM. The dashed-solid line illustrates the boundaries where transition from droplet-matrix morphology changes to spinodal and vice versa

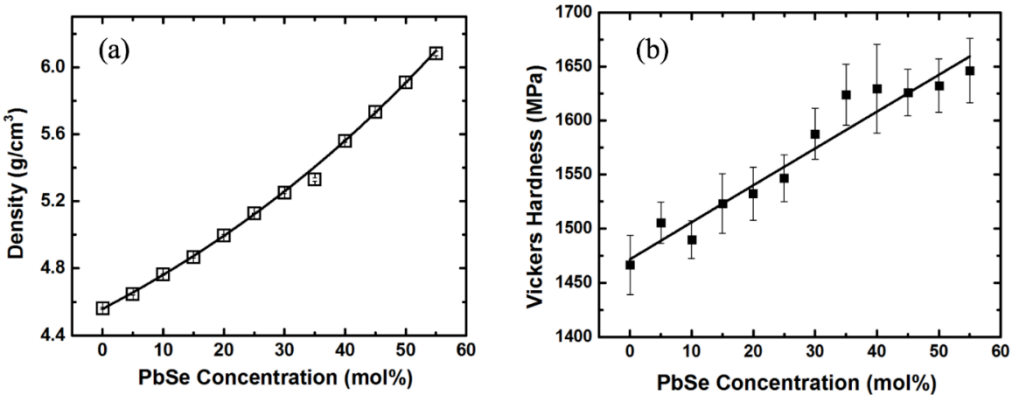

Figure 8. Variation of (a) density and (b) Vickers hardness with PbSe content in the $(GeSe_2–3As_2Se_3)_{1-x}PbSe_x$ [GAP-Se] glass system. Where not shown, error is within the size of the points

after 25 mol% PbSe (Figure 7 (a)). This suggests that Pb serves to modify the Ge–Se–As network up to this 25 mol% and that beyond this level, the Pb takes a different role in the glass structure, likely as a network participant in the Pb-rich matrix that starts to appear near this PbSe level. This transition is again consistent with the abrupt change observed in both the morphology (TEM) and the composition (XEDS). This change in role is further supported by the striking features of the series' spectra highlighted in Figure 7(b); the rise of the 800 cm^{-1} band with increasing PbSe concentration. Again, in both plots, the dashed lines (shown as a guide to the eye) shows the changes up to the point where at ~25–30% the glass' network becomes uniformly Pb-containing to Pb-rich and the role of Pb is likely more of a formal network participant.

We interpret the observation of three regions to the following structural changes. As the concentration of PbSe increases, the number of coupled $GeSe_4$ and $AsSe_{3/2}$ pyramidal structural unit decrease as will the normalized intensity of 230 cm^{-1}. While the $AsSe_{3/2}$ mode gradually decreases in intensity, the emergence of new bond corresponding to PbSe has become more visible for higher Pb content. In contrast to earlier Raman studies,[32,33] the present investigation shows explicitly the existence of vibrational modes corresponding to Ge–Se, As–Se and Pb–Se and its variation with Pb content. In the mid-PbSe regime (25–30 mol%) the plateau appears indicative of a transition region which could be associated with the inflection from a Pb-deficient matrix to a Pb-rich matrix as the dominant phase, through the spinodal range. This is likely the position of the 'top' of the immiscibility dome shown schematically above. The high PbSe regime supports the conclusion that beyond this level (>~35 mol% PbSe) the Pb addition to the network no longer impacts the glass' original Ge–As–Se backbone, but rather, directly participates in the network likely taking on more of an intermediate role.

The structural variation associated with the transition behaviour of Pb in the glass network is supported in other physical property measurements. Figure 8(a) and (b) shows the density and Vickers hardness as a function of increasing PbSe concentration, both exhibiting a monotonic increase with Pb levels. The density of glass increases as content of PbSe increases; from 4·562 g/cm^3 for 0 mol% PbSe to 6·081 g/cm^3 for 55 mol% PbSe. The increase in the density is attributed to the heavier atomic weight of Pb element and the increased packing of the Pb atom into the free volume of the glass network. The Vickers hardness H_V of glasses while related to the bond dissociation energy per unit volume of the components is also defined by the molar volume of glass. As seen from Figure 8(b), the Vickers hardness increases linearly as concentration of PbSe increases. Even though the

Table 3. Summary of physical properties of the $(GeSe_2–3As_2Se_3)_{1-x}PbSe_x$ [GAP-Se] glasses

Sample (mol% PbSe)	*T_g (°C) (±2°C)*	*T_x (°C) (±2°C)*	*ΔT (°C) (±2·8°C)*	*Density (g/cm^3)*	*Hardness (MPa)*	*Thermal conductivity (W/mK)*
0	210·0	-	-	4·562	1466·57	0·223
5	207·0	310·0	103	4·647	1505·47	0·226
10	205·6	302·6	97·0	4·764	1489·89	0·227
15	204·0	302·9	98·9	4·867	1523·15	0·231
20	202·6	294·4	91·8	4·997	1532·33	0·231
25	202·7	285·8	83·1	5·127	1546·52	0·233
30	200·5	276·1	75·6	5·253	1587·78	0·238
35	200·4	260·2	59·8	5·33	1624·06	0·244
40	201·9	244·9	43·0	5·559	1629·69	0·247
45	202·7	246·0	43·3	5·732	1626·00	0·251
50	205·4	237·4	32·0	5·908	1632·51	-
55	207·7	230·8	23·1	6·081	1646·54	0·254

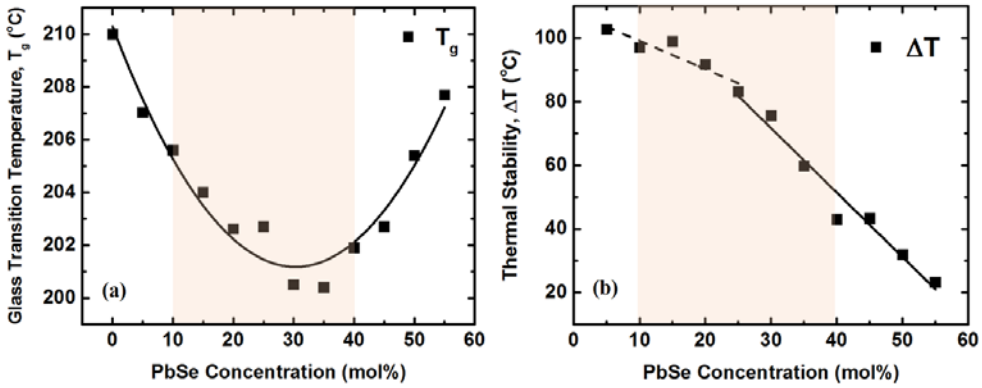

Figure 9. (a) Glass transition temperature, T_g, and (b) thermal stability ($\Delta T=T_x-T_g$) as a function of PbSe concentration. The shaded region is where droplet/matrix morphology exists. The shaded area ($10\leq x\leq 40$ mol% PbSe) indicates the composition where phase separation was observed by TEM. The dashed-solid lines illustrate the boundaries where transition from droplet-matrix morphology changes to spinodal and vice versa and are intended as a guide to the eye of property trends

bond dissociation energy of Pb–Se bond is lower than the Ge–Se and As–Se, the high atomic packing density with increasing PbSe compensates the lower dissociation energy and increases the hardness.

Table 3 summarizes the characteristic temperatures T_g, T_x, ΔT derived from DSC curves and density, microhardness and thermal conductivity. The network and morphological variation also translates to changes in thermal properties. Figure 9 shows the composition dependent variation of glass transition temperature (T_g) and thermal stability ($\Delta T=T_g-T_x$) for the glass series. It is seen that T_g for all the glass compositions follows a parabolic curve that appears to track with the immiscibility dome, as illustrated in Figure 9(a). The decrease in T_g through the perceived inflection point near ~30 mol%, can be associated with a transition from a low lead containing matrix (recall, Pb is concentrated in the Pb-rich droplets), to the point where Pb is contained largely in the dominant Pb-rich matrix. Similar changes are seen in Pb-oxide 'flint' optical glasses where thermal and mechanical properties were seen to transition when Pb moved from a modifier to a network role.[51] Additionally, glass stability degrades when Pb is a major network participant, in the Pb-rich matrix region. In the same ~30 mol% region, the compositional similarity of the two phases is evident in the apparent minima plateau of T_g before rising again. As can be seen, with increasing PbSe concentrations ΔT continuously degrades, initially slowly while Pb modifies the network in the homogeneous glass, and becoming more rapid as it starts to integrate into both the Pb-deficient and Pb-rich matrix (above ~25%). This change of slope is again, consistent with a change of morphology seen as the glasses approach the spinodal region where the compositional variation on stability is driven by the dominant matrix (Pb-rich) phase.

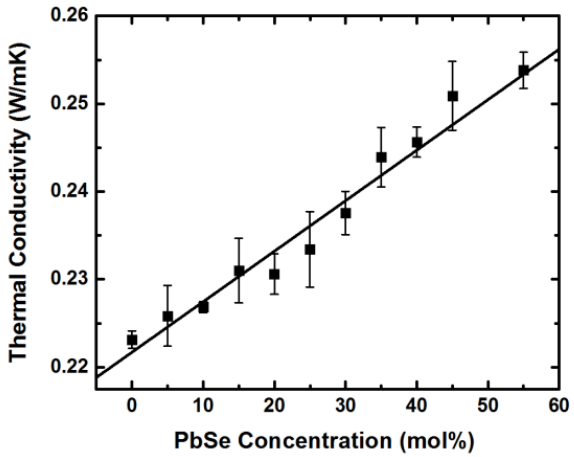

Figure 10. Change in the value of thermal conductivity of glasses with addition of PbSe

Figure 10 shows the evolution of thermal conductivity which increases linearly with increasing concentration of PbSe. The thermal conductivity enhancement seen may be interpreted as due to two reasons: (i) introduction of highly conductive element Pb, and (ii) the corresponding increase in the refractive index. When the Pb volume fraction increases, the Pb's superior thermal conductivity increases the overall thermal conductivity of glass system. Also, the dominant photon contribution to the thermal conductivity K_p, is directly related to the refractive index as,

$$K_p = \frac{16}{3}\frac{\sigma n^2 T^3}{\alpha}$$

where σ is the Stephan–Boltzmann constant, n is the refractive index, T is the temperature, and α is the absorption coefficient for the material.[52,53] As discussed in Ref. 42, the refractive index for these glasses increases as the concentration of the PbSe increases which may be expected to lead to the observed increase in the thermal conductivity.[42]

4. Conclusions

The morphology and physical properties of glasses in the $(GeSe_2–3As_2Se_3)_{1-x}PbSe_x$ [GAP-Se] system with varying PbSe concentration were investigated. Liquid–liquid phase separation (LLPS) was experimentally observed (between PbSe levels of x=10–45 mol%) and the amorphous nature of phases seen were confirmed by XRD. Depending on the glass composition, droplet-matrix or spinodal-like morphology was observed, with a transition region (correlated with the transition in composition of the liquid phases near 25–30 mol% PbSe) which separates the Pb-deficient matrix and Pb-rich matrix regimes. Optical transmission was directly correlated to phase morphology (droplet size) and composition (Pb-level) and the similar composition of the two glassy phases in the 30 mol% glass supports the lack of scattering and good transmission observed. The results suggest that Pb transitions from a modifier role at low levels (when present in Pb-rich droplets) to that of a network participant in higher PbSe compositions where it is incorporated in the Ge–As–Se network. These transition points have been validated by physical property measurements and Raman spectroscopy. Increasing levels of PbSe results in the significant increase in the density, microhardness and thermal conductivity of glasses, at the expense of glass stability to devitrification. Understanding the influence of phase separation on structure and properties relation can offer new possibilities to the ability to design new compositions and advanced composite materials.

Acknowledgment

This work was supported in part by Defense Advanced Research Projects Agency under Air Force Research Laboratory contract FA8650-12-C-7225 through the M-GRIN Tech Area 2 program. The views, opinions and/or findings expressed are those of the author and should not be interpreted as representing the official views or policies of the Department of Defense or the US Government. The authors acknowledge the helpful insight from discussions with Professor Edgar Zanotto. This document has been approved for publication release with unlimited distribution.

References

1. Seddon, A. B. Chalcogenide glasses: a review of their preparation, properties and applications. *J. Non-Cryst. Solids*, 1995, **184**, 44–50.
2. Guin, J. P., Rouxel, T., Sanglebœuf, J. C., Melscoët, I. & Lucas J. Hardness, toughness, and scratchability of germanium–selenium chalcogenide glasses. *J. Am. Ceram. Soc.*, 2002, **85** (6), 1545–1552.
3. Varshneya, A. K. Some comments on physical properties of chalcogenide glasses. *J. Non-Cryst. Solids*, 2000, **273** (1), 1–7.
4. Partridge, G. Glass-ceramics with unusual electrical properties. *Adv. Mater.*, 1992, **4** (10), 668–673.
5. Chevalier, J. & Gremillard, L. Ceramics for medical applications: A picture for the next 20 years. *J. Eur. Ceram. Soc.*, 2009, **29** (7), 1245–1255.
6. Rawlings, R. D., Wu, J. P. & Boccaccini, A. R. Glass-ceramics: their production from wastes—a review. *J. Mater. Sci.*, 2006, **41** (3), 733–761.
7. Seznec, V., Ma, H. L., Zhang, X. H., Nazabal, V., Adam, J. L., Qiao, X. S. & Fan. X. P. Preparation and luminescence of new Nd^{3+} doped chloro-sulphide glass-ceramics. *Opt. Mater.*, 2006, **29** (4), 371–376.
8. Balda, R., Garcia-Revilla, S., Fernández, J., Seznec, V., Nazabal, V., Zhang, X. H., Adam, J. L., Allix, M. & Matzen. G. Upconversion luminescence of transparent Er^{3+}-doped chalcohalide glass–ceramics. *Opt. Mater.*, 2009, **31** (5), 760–764.
9. Donald, I. W. Preparation, properties and chemistry of glass-and glass-ceramic-to-metal seals and coatings. *J. Mater. Sci.*, 1993, **28** (11), 2841–2886.
10. Tick, P. A., Borrelli, N. F., Cornelius, L. K. & Newhouse M. A. Transparent glass ceramics for 1300 nm amplifier applications. *J. Appl. Phys.*, 1995, **78** (11), 6367–6374.
11. Zanotto, E. D. Bright future for glass-ceramics. *Am. Ceram. Soc. Bull.*, 2010, **89** (8), 19–27.
12. Wolfram, H. & Beall G. H. *Glass Ceramic Technology*. John Wiley & Sons, 2012.
13. McCloy, J. S., Riley, B. J., Pierce, D., Johnson, B. R. & Qiao, A. Infrared-transmitting glass-ceramics: A review. *SPIE Defense, Security, and Sensing*, International Society for Optics and Photonics, 2013, 87080N–87080N.
14. McCloy, J. S., Riley, B. J. & Pierce, D. A. Infrared-transparent glass ceramics: An exploratory study. *J. Non-Cryst. Solids*, 2015, **410**, 160–173.
15. Ma, H., Zhang, X. & Lucas, J. Infrared transmitting chalcogenide glass ceramics. *J. Non-Cryst. Solids*, 2003, **317** (3), 270–274.
16. Moynihan, C. T., Macedo, P. B., Aggarwal, I. D. & Schnaus, U. E. Direct observation of the double glass transition in a phase-separated glass. *J. Non-Cryst. Solids*, 1971, **6** (4), 322–328.
17. Shaw, R. R. & Uhlmann, D. R. Effect of phase separation on the properties of simple glasses I. Density and molar volume. *J. Non-Cryst. Solids*, 1969, **1** (6), 474–498.
18. Neuville, D. R., Cormier, L., Caurant, D. & Montagne, L.*From glass to crystal–Nucleation, growth and phase separation, from research to applications*, EDP Sciences, Les Ulis, France, 2017, Chapter 17.
19. *Ibid*, Chapter 19.
20. *Ibid*, Chapter 21.
21. Kokorina, V. F. *Glasses for Infrared Optics*, *CRC Press*, 1996
22. Zanotto, E. D. *Crystals in glass: a hidden beauty*, John Wiley & Sons, 2013.
23. Neuville, D. R., Cormier, L., Caurant, D. & Montagne, L. *From glass to crystal–Nucleation, growth and phase separation, from research to applications*, EDP Sciences, Les Ulis, France, 2017.
24. *Ibid*, Chapter 4.
25. Shelby, J. E. *Introduction to glass science and technology*. Royal Society of Chemistry, 2005.
26. Zhang, X. H., Calvez, L., Seznec, V., Ma, H. L., Danto, S., Houizot, P., Boussard-Plédel, C. & Lucas, J. Infrared transmitting glasses and glass-ceramics. *J. Non-Cryst. Solids*, 2006, **352** (23), 2411–2415.
27. Mecholsky J. J., Srinivasan, G. R., Moynihan, C. T. & Macedo, P. B. Immiscibility and liquidus temperatures in the pseudobinary chalcogenide system $PbSeGe_{1.5}As_{0.5}Se_3$. *J. Non-Cryst. Solids*, 1973, **11** (4), 331–340.
28. Mecholsky, J. J., Moynihan, C. T., Macedo, P. B. & Srinivasan, G. R. Microstructure and properties of an infra-red transmitting chalcogenide glass-ceramic. *J. Mater. Sci.*, 1976, **11** (10), 1952–1960.
29. Mecholsky, J. J. Microstructural Investigations of a Chalcogenide Glass Ceramic. PhD Thesis, 1973.
30. Kyriazis, F., Chrissanthopoulos, A., Dracopoulos, V., Krbal, M., Wagner, T., Frumar, M. & Yannopoulos, S. N. Effect of silver doping on the structure and phase separation of sulfur-rich As–S glasses: Raman and SEM studies. *J. Non-Cryst. Solids*, 2009, **355** (37), 2010–2014.
31. Zhang, Z.H., Kennedy, J. H., Thompson, J., Anderson, S., Lathrop, D. A. & Eckert, H. Competitive network modification in non-oxide chalcogenide glasses structural and motional properties of glasses in the system Li_2S-P_2S_5-B_2S_3 studied by multinuclear NMR techniques. *Appl. Phys. A: Mater. Sci. Process.*, 1989, **49** (1), 41–54.
32. Wang, H., Zhang, X., Yang, G., Xu, Y., Ma, H., Adam, J. L., Gu, Z. & Chen. G. Micro-crystallization of the infrared transmitting chalcogenide glass in $GeSe_2$–As_2Se_3–PbSe system. *Ceram. Int.*, 2009, **35** (1), 83–86.
33. Yang, G., Zhang, X., Ren, J., Yunxia, Y., Chen, G., Ma, H. & Adam, J. L. Glass formation and properties of chalcogenides in a $GeSe_2$–As_2Se_3–PbSe system. *J. Am. Ceram. Soc.*, 2007, **90** (5), 1500–1503.
34. Xia, F., Zhang, X., Ren, J., Chen, G., Ma, H. & Adam, J. L. Glass formation and crystallization behavior of a novel GeS_2–Sb_2S_3–PbS chalcogenide glass system. *J. Am. Ceram. Soc.*, 2006, **89** (7), 2154–2157
35. Donghui, Z., Fang, X., Guorong, C., Xianghua, Z., Hongli, M. & Adam, J. L. Formation and properties of chalcogenide glasses in the

$GeSe_2$–As_2Se_3–CdSe system. *J. Am. Ceram. Soc.*, 2005, **88** (11), 3143–3146.
36. Wang, G., Li, C., Nie, Q., Pan, Z., Li, M., Xu, Y., Wang, H. & Shi, D. Thermal stability and far infrared transmitting property of $GeTe_4$-$AsTe_3$-AgI glasses and glass-ceramics. *J. Non-Cryst. Solids*, 2017, **463**, 80–84.
37. Lin, C., Calvez, L., Rozé, M., Tao, H., Zhang, X. & Zhao, X. Crystallization behavior of 80GeS_2-20Ga_2S_3 chalcogenide glass. *Appl. Phys. A: Mater. Sci. & Process*, 2009, **97** (3), 713–720.
38. Lin, C., Calvez, L., Tao, H., Allix, M., Moréac, A., Zhang, X. & Zhao, X. Evidence of network demixing in GeS_2–Ga_2S_3 chalcogenide glasses: a phase transformation study. *J. Solid State Chem.* 2011, **184** (3), 584–588.
39. Gustafsson, S. E. Transient plane source techniques for thermal conductivity and thermal diffusivity measurements of solid materials. *Rev. Sci. Instrum.*, 1991, **62** (3), 797–804.
40. Singh, K., Patidar, D. & Saxena, N. S. Composition dependence of effective thermal conductivity and effective thermal diffusivity of $Se_{100-x}In_x$ (x= 0, 5, 10, 15 and 20) chalcogenide glasses. *J. Phys. Chem. Solids*, 2005, **66** (6), 946–948.
41. Lonergan, J., Smith, C., McClane, D. & Richardson, K. Thermophysical properties and conduction mechanisms in As_xSe_{1-x} chalcogenide glasses ranging from x= 0.2 to 0.5. *J. Appl. Phys.*, 2016, **120** (14), 145101.
42. Sisken, L., Smith, C., Buff, A., Kim, M., Chamma, K. , Wachtel, P., Musgraves, J. D., Rivero-Baleine, C., Kirk, A., Kalinowski, M., Melvin, M. & Richardson K. Evidence of spatially selective refractive index modification in 15$GeSe_2$-45As_2Se_3-40PbSe glass-ceramic through correlation of structure and optical property measurements for GRIN applications. *Opt. Mater. Expr.*, 2017, in press.
43. Buff, A. K. A Study of Crystallization Behavior in Phase Separated Chalcogenide Glasses. MSc. Thesis, Department of Materials Science and Engineering, University of Central Florida, 2016.
44. Ikari, T., Tanaka, T., Ura, K., Maeda, K., Futagami, K. & Shigetomi, S. Raman spectra of P-, Sb-, or Bi-doped Ge_xSe_{1-x} bulk glasses. *Phys. Rev. B*, 1993, **47** (9), 4984
45. Boolchand, P., Feng, X. & Bresser, W. J. Rigidity transitions in binary Ge–Se glasses and the intermediate phase. *J. Non-Cryst. Solids* 2001, **293**, 348–356.
46. Barney, E. R., Abdel-Moneim, N.S., Towey, J. J., Titman, J., McCarthy, J. E., Bookey, H. T., Kar, A., Furniss, D. & Seddon, A. B. Correlating structure with non-linear optical properties in x$As_{40}Se_{60}$·(1− x)$As_{40}S_{60}$ glasses. *Phys. Chem. Chem. Phys.* 2015, **17** (9), 6314–6327.
47. Li, W., Seal, S., Rivero, C., Lopez, C., Richardson, K., Pope, A., Schulte, A., Myneni, S., Jain, H., Antoine K. & Miller, A. C. Role of S:Se ratio in chemical bonding of As–S–Se glasses investigated by Raman, x-ray photoelectron, and extended x-ray absorption fine structure spectroscopies. *J. Appl. Phys.*, 2005, **98** (5) 053503.
48. Yang, A. L., Hui-Zhen, W., Zhi-Feng, L., Dong-Jiang, Q., Yong, C., Jian-Feng, L., McCann, P. J. & Fang, X. M. Raman scattering study of PbSe grown on (111) BaF2 substrate. *Chin. Phys. Lett.* 2000, **17** (8), 606.
49. Alvi, M. A. & Khan, Z. H. Synthesis and characterization of nanoparticle thin films of a-$(PbSe)_{100-x}Cd_x$ lead chalcogenides. *Nanoscale Res. Lett.*, 2013, **8** (1), 1–10.
50. Sen, R. I., Singh, R. K., Singh, P. & Singh, K. Effect of Pb addition on dielectric relaxation in Se 80 In 20 glassy system. *J. Alloys Compd.*, 2013, **552**, 480–485.
51. McKinley, J. M. The role of lead in the structure, properties, and cnc microgrinding of alkali lead silicate glasses. MSc. Thesis, Department of Mechanical, Materials and Aerospace Engineering, University of Central Florida, 1996.
52. Lonergan, J., Smith, C., McClane, D. & Richardson, K. Thermophysical properties and conduction mechanisms in AsxSe1−x chalcogenide glasses ranging from x= 0.2 to 0.5. *J. Appl. Phys.*, 2016, **120** (14), 145101.
53. Hayes, D. J., Rea, S. N. & Hilton, A. R. Thermal conductivity of infrared transparent chalcogenide glasses. *J. Am. Ceram. Soc.*, 1975, **58** (3–4), 135–137.